Thin Solid Films 546 (2013) 347–352

Contents lists available at ScienceDirect

Thin Solid Films

journal homepage: www.elsevier.com/locate/tsf

Fabrication of large-scale single-crystal Cu(In,Ga)Se_2 nanotip arrays solar cell by one-step ion milling processes

Yi-Chung Wang [a,c,1], Yu-Ting Yen [a,c,1], Chin-Hung Liu [a,c], Chia-Hsiang Chen [a], Wei-Chen Kuo [b], Jenh-Yih Juang [b], Chih-Huang Lai [a], Yu-Lun Chueh [a,c,*]

[a] Department of Materials Science and Engineering, National Tsing Hua University, Hsinchu, 30013, Taiwan, ROC
[b] Department of Electrophysics, National Chiao Tung University, Hsinchu, 30013, Taiwan, ROC
[c] Center For Nanotechnology, Material Science, and Microsystem, National Tsing Hua University, No. 101, Sec. 2, Kuang-Fu Rd., Hsinchu 30013, Taiwan, ROC

ARTICLE INFO

Available online 9 May 2013

Keywords:
CIGS solar cells
Nanostructure
Nanotip arrays
Photovoltaic
KCN washing
CdS layer
Post-selenization process

ABSTRACT

Template-free, one step formation of Cu(In, Ga)Se_2 (CIGS) nanotip arrays (NTRs) to enhance device efficiency were discussed. Through Ar^+ ion milling process, the CIGS NTRs could be formed directly on the CIGS layer. The angles and lengths of CIGS NTRs could be precisely controlled by incident angle of Ar^+ beam and milling time, respectively. Mechanisms were proposed to be a self-masking effect by Cu segregation formed at early stage confirmed by Transmission Electron Microscopy, Grazing Incidence X-ray Diffraction, Energy Dispersive Spectroscopy, and Auger Electron Spectroscopy. Measurements of devices on various KCN washing time and thickness of CdS buffer layer were reported to achieve the highest efficiency of CIGS NTRs devices. This approach provides one-step fast process without templates, easy integration with in-line sputtering process, and no post-selenizatoin process for the formation of CIGS nanostructure, which can stimulate great attention not only in academic investigations but also in industrial side for practical applications.

1. Introduction

Issues related to global warming and limited sources of fossil fuel have threatened the existence of human being. Thus, searching for alternative, renewable and clean energy is an urgent demand, which has recently attracted enormous attention of the scientists worldwide. Among the renewable alternative energies being explored, solar energy is considered as one of the most promising candidates while developing efficient solar cells has become a potential challenge for converting solar energy into electrical energy to satisfy the growing demand. Among the materials as the solar cell, Cu($In_xGa_{(1-x)}$)Se_2 (CIGS) has attracted much attention because of its high conversion efficiency of ~20.3% [1]. CIGS has a near optimal and tunable band gap *via* band gap engineering [2,3], which further enhances its ability for light absorption and carriers collection. To reduce the material cost, the reduction of the thickness of the absorber, namely CIGS layer, should be considered, with which the efficiency still remains intact. However, the critical issue encountered is that the long wavelength region of the solar spectrum cannot be fully absorbed as the absorber thickness is reduced, resulting in diminishing of a short circuit current, J_{SC} [4]. To overcome this problem, there is strong eager to develop all kinds of light trapping approach to enhance carrier generation even under an ultra-thin absorber circumstance.

Up to date, schemes based on nanostructures for light absorption or light trapping have been applied on silicon-based solar cells. For example, honeycomb nanostructure in Si-based photovoltaic (PV) devices, which has benefits on intrinsic self-clean property, efficiency enhancement and thinner absorber thickness. It has been used to enhance cell performance from 18.6% to 19.8% [5,6]. Unfortunately, owing to the quaternary composition, very few studies on light trapping schemes based on the formation of nanostructured CIGS were found. In this regard, we demonstrate a low-cost, template-free and non-toxic method to fabricate large area and uniform CIGS nanostructures, namely CIGS nanotip arrays (NTRs) from CIGS thin films (TF) *via* a direct sputtering of a CIGS target without a post-selenization process, which enables the exploration another branch of the nanostructured CIGS solar cell. To figure out the ion milling parameters, we analyzed the CIGS NTRs in morphology, structural and compositional changes. As studied before, the effect of KCN washing and the buffer layer thickness is critical processes for the performance of the CIGS solar cells [7–10]. Therefore, the effects of KCN washing time and CdS thicknesses on the CIGS NTRs were investigated in order to optimize the performance of the CIGS solar cell.

* Corresponding author at: Department of Materials Science and Engineering, National Tsing Hua University, Hsinchu, 30013, Taiwan, ROC. Tel.: +886 35715131x33965.
E-mail address: ylchueh@mx.nthu.edu.tw (Y.-L. Chueh).
[1] These authors contribute equally to this work.

0040-6090/$ – see front matter.
http://dx.doi.org/10.1016/j.tsf.2013.04.085

2. Experimental procedures

2.1. Sputtering of CIGS TF without post-selenization process

The CIGS layers were fabricated by using a sputtering system with four 2-inch magnetron sputtering guns and a rotatable substrate holder with heating apparatus. Back molybdenum electrode with thickness of 1 μm was deposited on a pre-cleaned 2×2 cm^2 soda-lime glass substrate by DC magnetron sputtering. CIGS films with the chalcopyrite phase were deposited by direct sputtering of a single quaternary CIGS target. The CIGS quaternary target has compositions of Cu, In, Ga, and Se being of 25, 17.5, 7.5 and 50 at %, respectively. The sputtering chamber was pumped down to a base pressure of 1.33×10^{4} Pa before deposition. The working pressure during the deposition was 4.00×10^{-1} Pa with pure Ar gas. CIGS films were deposited by pulse DC magnetron sputtering at 500 °C.

2.2. Formation of CIGS NTRs by ion milling processes

Fig. 1A shows how we create the CIGS NTRs. The samples were placed inside a 4-in ion miller with a single tilting stage, which is able to adjust the incident angle of Ar^{+} ions from 15° to 90°. The base pressure was pumped down to 4×10^{-4} Pa and the working pressure during milling processes was kept at 1.60×10^{-2} Pa. We set the filament current at 3.85 A, the beam voltage at 400 V, the accelerator voltage at 300 V, and the beam current at 50 mA, respectively.

2.3. KCN washing treatment

KCN washing was applied on both TF and NTRs before cell preparation. Stock solution was made by potassium cyanide, KCN (ACROS, 97%) with 10 wt % in water solution. Both CIGS TF and NTRs was immersed into stock solution in 5, 7, 15 and 20 min respectively. The KCN-treated samples were then washed by running deionized water and purged by nitrogen gas for device fabrication.

2.4. Deposition of CdS layer via chemical bath deposition

CdS deposition was applied on the surface of the nanostructural CIGS layer immediately after KCN washing via chemical bath deposition (CBD). Cadmium sulfate 8/3-hydrate, $CdSO_4 \cdot 8/3H_2O$ (Sigma-Aldrich, 99%), thiourea, $CS(NH_2)_2$ (Sigma-Aldrich, 99 + %) and ammonium hydroxide solution, NH_4OH (JT baker, 28.0–30.0%) are chemicals applied in this process. For detail, CdS layer was prepared by mixing the solution of 0.5 mM cadmium sulfate 8/3-hydrate, 75 mM thiourea and ammonium hydroxide solution 3.11 M, respectively. Then, CIGS NTRs sample was immersed into a mixing solution within an air-tight container and then heated to 60 °C for deposition of CdS layer at different time.

2.5. Device fabrication processes

A 100 nm-thick intrinsic zinc oxide insulating layer and a 200 nm-thick aluminum-doped zinc oxide were deposited on the CdS/CIGS NTRs sample by RF magnetron sputtering. The 1 μm top Al grid

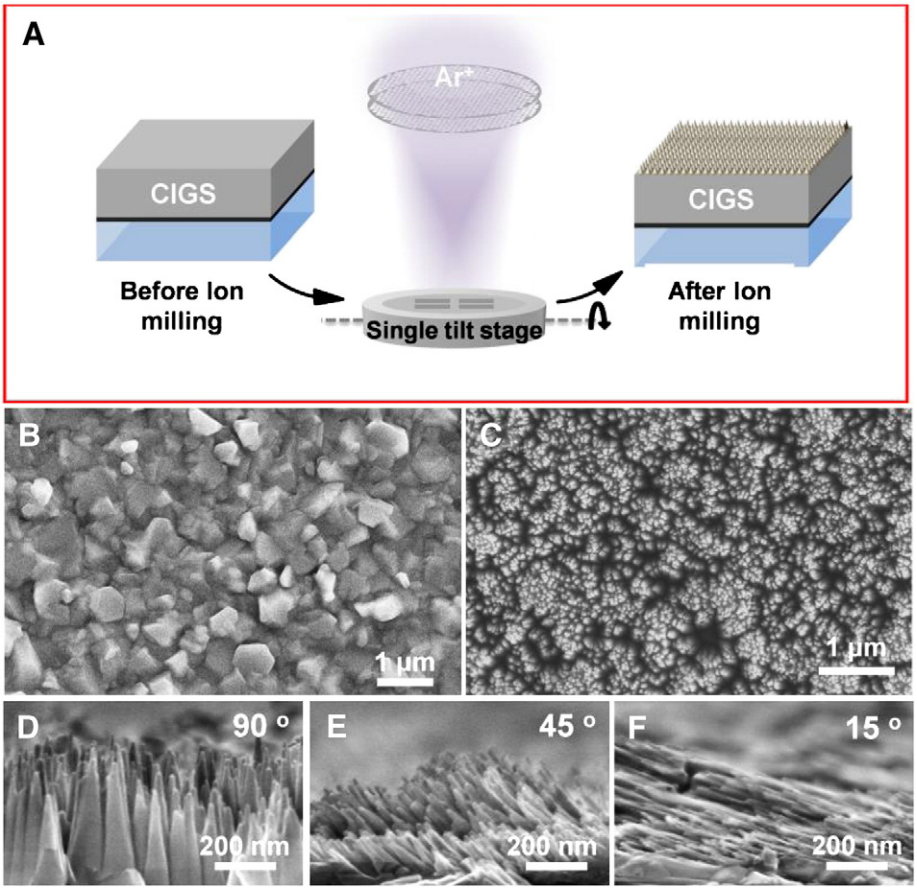

Fig. 1. (A) Schematic of the ion milling process. A CIGS TF sample was placed on a single tilting stage inside a 4-inch ion miller with a 400 eV Ar^{+} ion beam. SEM images of CISG TF sample before (B) ion milling and after (C) ion milling at 90° with 30 min, The cross-section SEM images of the CIGS TFs after ion milling at (D) 90°, (E) 45°, and (F) 15° with 30 min, respectively.

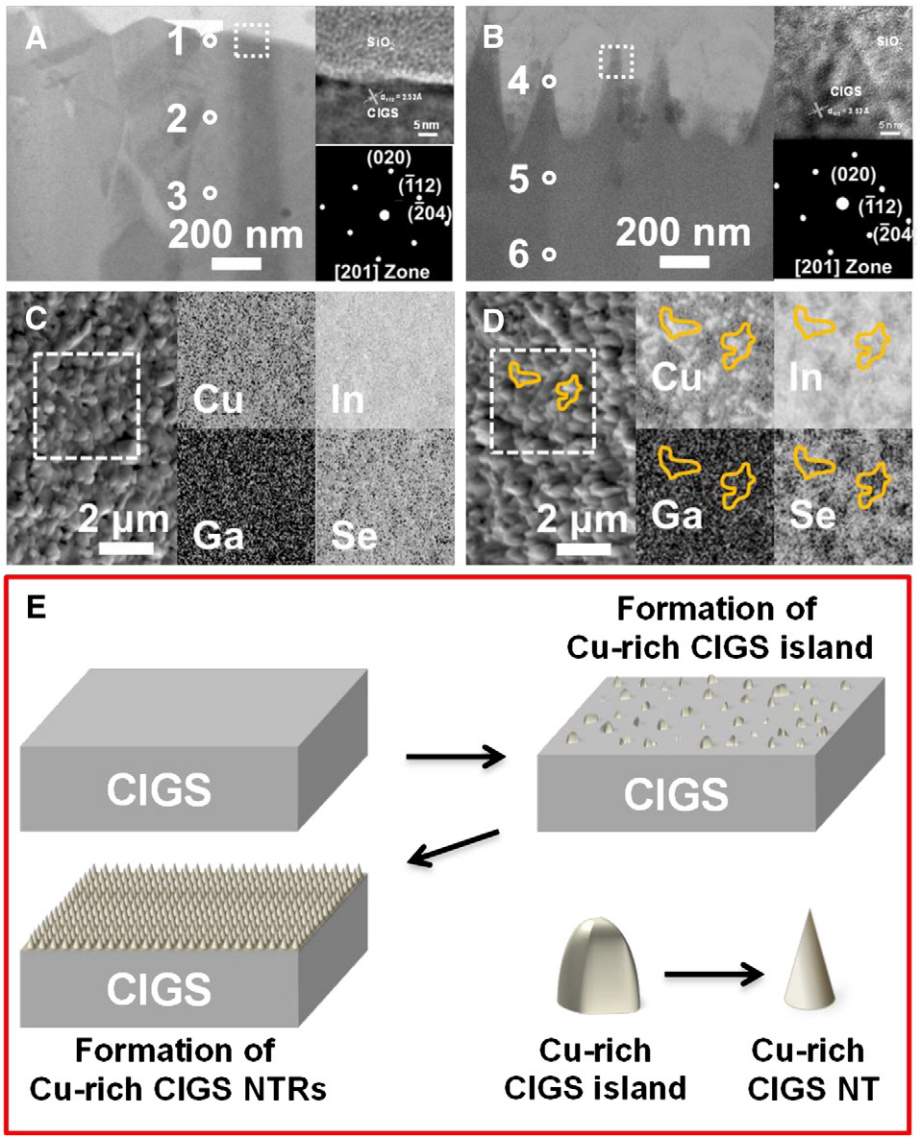

Fig. 2. Cross-section TEM images of (A) CIGS TF and (B) CIGS NTRs. Insets show the corresponding HRTEM images and selected area diffraction patterns. The marked positions from 1 to 6 are used to obtain the EDS results as listed in Table 1. AES mapping of (C) CIGS TF and (D) CIGS NTRs. (E) The possible mechanism for formation of CIGS NTRs.

electrodes were prepared by e-gun evaporation with a contact hard mask to form a complete device with a 0.5 cm^2 cell area.

2.6. Characterization

Crystal structures of the CIGS films were characterized by a Grazing Incident Angle XRD (GIXRD) with Cu Kα (λ = 0.154 nm) as the radiation source. The scan range starts from 20° to 80° with a scan rate of 4°/min and an incident angle of 1°. Morphologies and microstructures were studied by field-emission scanning electron microscopy (SEM, JSM-6500F, JEOL) and transmission electron microscopy (TEM, JEM-3000F, JEOL) with operating voltages at 15 kV and 300 kV respectively. TEM specimens were prepared by focus ion beam technique through gallium as ion source. The samples were thinned down to ~200 nm thick followed by *in situ* lift out process (Note: Extreme care must be taken while overdose of gallium ion may damage the samples.) to transfer specimen onto carbon-supported Ni grid for characterizations. The density of CIGS NTRs was examined by atomic force microscopy (Di-3000, Vecco). Composition of CIGS NTRs was characterized with an energy dispersive spectrometer (EDS) attached to the TEM. The current–voltage characteristics and external quantum efficiency (EQE) of PV devices were measured by Keitheley 4200 analyzer under AM 1.5 solar illumination with the power density of 100 mW/cm^2 at 25 °C using a Xe arc lamp as the light source.

Table 1
Quantitative analysis obtained with an energy dispersive spectrometer (EDS). Points 1 to 6 correspond to positions in Fig. 2(A) and (B). At % means atomic percentage.

	Cu at%	In at%	Ga at%	Se at%
1	28	20	9	43
2	25	18	13	44
3	23	20	12	45
4	50	9	8	33
5	24	20	9	47
6	24	19	11	46

3. Results and discussion

3.1. Structural analysis (SEM, TEM)

By applying Ar^+ ion milling process, we could fabricate CIGS nanostructure in a large area with a high throughput (4-inch substrate size

for the ion miller). As we can see from Fig. 1(B) and (C), the pristine CIGS TF could be turned into NTRs after the ion milling process. Interestingly, apex angles of CIGS NTRs are controllable, depending on the ions incident angle as shown in Fig. 1(D) to (F), providing an excellent controllability of nanostructure. In addition, we found that the length of CIGS NTRs were ~140 nm, ~160 nm, ~320 nm, ~190 nm and ~120 nm for the ion milling time of 10, 20, 30, 60 and 90 min respectively, indicating that the length of CIGS NTRs increases as the ion sputtering time increases while a maximum length was achieved at the milling time of 30 min.

To understand crystalline quality of the CIGS NTRs, TEM results are imperative. The cross-section TEM images of CIGS TF before and after the Ar^+ ion milling process with an incident angle of 90° for 10 min are shown in Fig. 2(A) and (B), respectively. The columnar structure CIGS TF deposited by sputtering process could be confirmed while vertical CIGS NTRs could be clearly observed after the Ar^+ ion milling process. Insets in Fig. 2(A) and (B) show the corresponding high-resolution TEM images and selected area diffraction, indicating the single-crystalline feature of the CIGS NTRs after the ion milling process. The compositional distributions of CIGS TF and CIGS NTRs samples were measured in Table 1, with which the corresponding positions are marked at positions from 1 to 6 in Fig. 2A and B, respectively. For CIGS TF, the atomic concentrations of [Cu], [In] + [Ga], and [Se] are in average to be ~25 at %, ~31 at %, and ~44 at %, respectively. Obvious deviations of compositions from the CIGS target to the deposited CISG film can be found, which is resulted from an unstable Se behavior due to low melting point where Se atoms can be easily be vaporized out of the deposited CIGS film during sputtering process, resulting in a less Se concentration in the deposited CIGS film. Notably, the EDS compositional analysis in Table 1 clearly shows the compositional difference between CIGS TF and CIGS NTRs. For CIGS TF, a slightly Cu-rich signal was observed through the entire film. However, CIGS NTRs showed an obviously higher Cu concentration near tip region. To confirm the composition distribution, AES mapping was applied to evaluate the concentration distribution of Cu, In, Ga, and Se as shown in Fig. 2C and D, respectively. The surface of CIGS TF shows an uniform distribution of each element (dash lines indicate the AES analysis regions) while some Cu-rich islands randomly located on the CIGS NTRs surface could be found, which also agree with the EDS analysis, pointing out a possible formation of Cu rich phase at tip region.

To shed light on the formation of the CIGS NTRs, we suggest the self-mask mechanism combined with Bradley–Harper model in the beginning stage of the ion-milling process to explain the formation of the CIGS NTRs [11]. Fig. 2E illustrates the formation process of CIGS NTRs. Once Ar^+ ions with high energy milling the surface of CIGS TF, Cu, In, Ga, and Se atoms will be sputtered away from the surface of the CIGS TF with different sputtering yields, with the order of Se > In > Cu > Ga [12]. Therefore, it results in some Cu-rich regions that remained on the surface as starting points for the formation of the tips. Then, the Cu-rich regions on the surface act as the mask preventing from Ar^+ ions bombardment. These highly Cu-rich CIGS nucleation sites, which are more resistant to ion milling than other regions, become a self-mask and lead to unequal milling rate around CIGS tip region, namely, anisotropic milling effect.

Based on the mechanism proposed above, the surface of the CIGS NTRs is quite different from CIGS TF either in morphological or compositional aspects, which should result in the different point of view from the typical CIGS PV process. As a result, it is necessary to develop optimum process to adapt roughness and Cu-rich surface caused by CIGS NTRs devices, which can be realized after KCN washing and deposition of CdS buffer layer.

Table 2
I–V behaviors of CIGS NTRs devices with different CdS thicknesses from 50 nm, 100 nm and 150 nm, respectively.

Thickness (nm)	V_{OC} (mV)	J_{SC} (mA/cm^2)	F.F. (%)	η (%)
50	50	11.43	25	0.1
100	390	22.56	59	5.2
150	180	5.55	30	1.4

3.2. Influence of KCN washing

Obviously, there were unwanted secondary phases, such as Cu-rich CIGS, Cu_2Se phases, which are consistent with our analysis results based on AES, GIXRD, and EDS of CIGS NTRs that appeared at the surface of CIGS NTRs after ion milling processes. KCN is treated as a well-known secondary phase eraser in the CIGS PV process [7,8]. Fig. 3A shows the GIXRD spectra of CIGS TF samples with different milling time. Obviously, it indicates invariant characteristics of chalcopyrite phase CIGS at different ion milling time while a distinct peak, namely Cu (111), owing to the segregation of Cu atoms after milling time > 30 min could be observed. Fig. 3B shows the GIXRD results of the 30 min milled CIGS NTRs samples before and after KCN washing at different washing time from 7 to 20 min, respectively. As can be seen in Fig. 3B, the best condition for removal of secondary

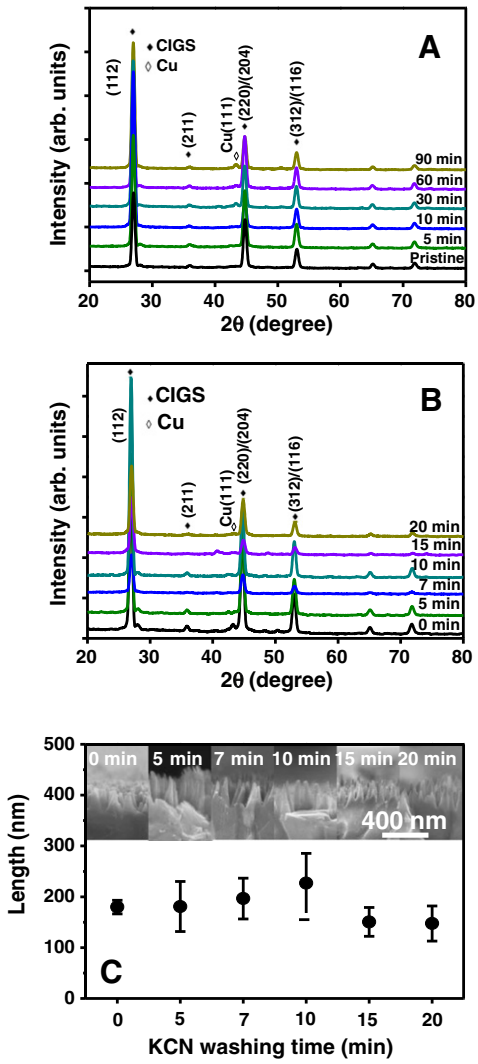

Fig. 3. (A) GIXRD spectra of CIGS NTRs prepared at different ion milling time. (B) GIXRD of the 30 min ion milled CIGS NTRs after different KCN washing time. (C) Length of 30 min ion milled CIGS NTRs as a function of KCN washing time. Inset shows the corresponding SEM images.

phase could be found as the KCN washing time over 20 min. In addition, we found that the length of CIGS NTRs increases as KCN treatment time increase and decreases after KCN washing time over 15 min, for which a maximum length of ~200 nm could be achieved as shown in Fig. 3C. The corresponding SEM images with different KCN washing time were shown in inset.

3.3. Influence of CdS thickness on CIGS NTRs

N-type CdS buffer layer deposited by CBD method is well-known for its superior coverage as a good interface passivation layer on the CIGS absorber. To obtain the highest device performance, different thicknesses from 50 to 150 nm of n-type CdS buffer layers were investigated. Fig. 4A to D show SEM images of CIGS NTRs before and after the deposition of CdS layers with thicknesses from 50 nm to 150 nm, respectively. Insets show the corresponding cross-sectional SEM images. Fig. 4E shows GIXRD results of the samples after deposition of CdS layers at different thicknesses from 50 to 150 nm. Note that the chalcopyrite phase of the CIGS remains intact after capping of the CdS layer, with which the CdS (100) peak could be identified. Fig. 4 F shows the corresponding I–V performance of the CIGS NTRs samples with different CdS layers of 50 nm, 100 nm and 150 nm, respectively and the corresponding V_{OC}, J_{SC}, FF, and conversion efficiency are shown in Table 2. Note that a very small efficiency of ~0.1% could be measured due to a large leakage current with the thickness of the CdS layer being 50 nm, which is consistent with SEM image. It reveals that the CdS layer is too thin to completely cover CIGS NTRs, leading to a lower shunt resistance. However, 150 nm-thick CdS layer suffers from high series resistance, resulting in a lower efficiency of only 1.4%. Therefore, the full coverage of the CdS layer with thickness of ~100 nm on the CIGS NTRs could be achieved and the highest performance could be measured with an open circuit voltage (V_{OC}) of ~390 mV and a short circuit current (J_{SC}) of 22.56 mA/cm^2, yielding an efficiency of 5.2% with a filling factor (FF) of 59% as shown in Fig. 5A. In contrast, CIGS TF device with the identical device configuration was prepared for comparison (Fig. 5A). The open circuit voltage and short circuit were measured to be 360 mV and 17.98 mA/cm^2 with the highest efficiency and the FF of 3.1% and 48%, respectively. Fig. 5B shows an EQE from 400 to 1300 nm, which provides the information of conversion efficiency for photon to electron–hole pairs (EPHs). The increased EQE response from wavelengths of 500 to 1000 nm could be attributed to the increase of effective light absorption ability to increase EPHs concentration, thereby enhancing J_{SC} and FF. In addition, the improved V_{OC} can be explained by the decrease of contact resistance due to the improvement of interfaces between CIGS NTRs/CdS [13]. Here, we provide one-step fast process with free of template, easy integration with in-line sputtering process, and no post-selenization process, which can stimulate great attention not only in academic investigations but also in industrial side for practical applications. In future, a control of (220)/(204) preferred orientation with desired compositions, reduction of secondary phase, control of Na concentration and modification of bandgap gradient to better benchmark efficiency than that of co-evaporation process are needed to improve our CIGS NTRs device. In addition, thickness of CdS layer, i-ZnO layer and interfaces of CIGS NTRs are required additional exploration.

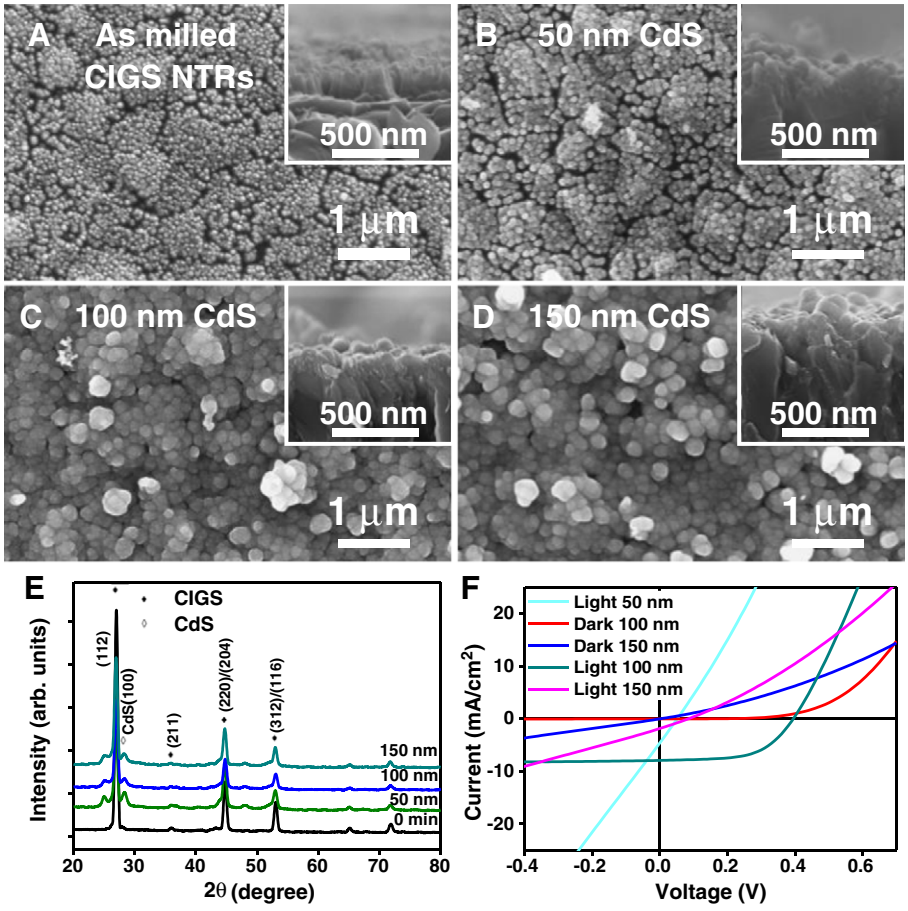

Fig. 4. SEM images of the CIGS NTRs samples (A) before capping of the CdS layer and after capping of the CdS layers with thicknesses of (B) 50 nm, (C) 100 nm, and (D) 150 nm, respectively. (E) GIXRD of CdS/CIGS NTRs with CdS of 50, 100, and 150 nm, respectively. (F) The corresponding I–V behaviors of CIGS NTRs devices with different thicknesses of the CdS layers.

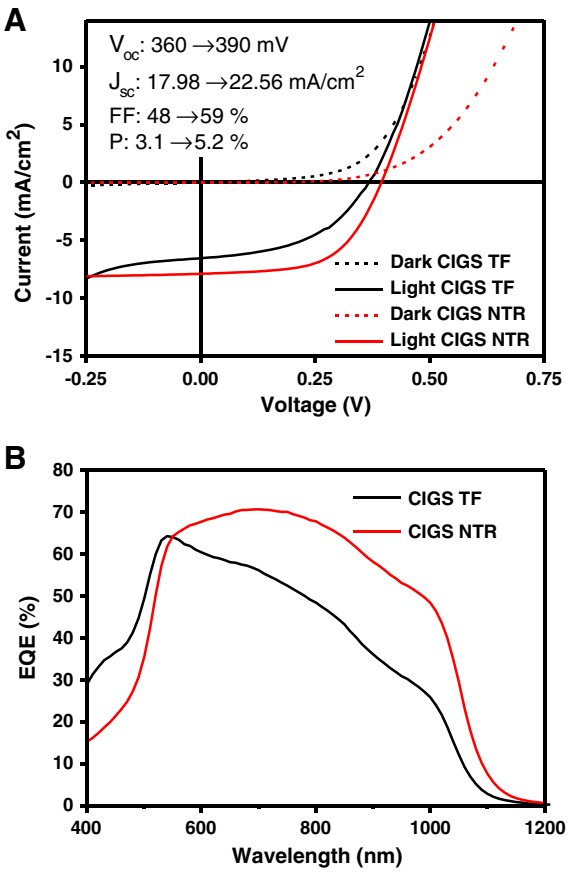

Fig. 5. (A) I–V behavior was measured using Keithley 4200 under the AM 1.5 illumination (100 mW/cm^2) at room temperature for both CIGS TFs and CIGS NTRs with the KCN washing time of 20 min. Best V_{oc}, J_{sc}, FF, and P for CIGS TF/CIGS NTRs device are 390/360 (mV), 22.56/17.98 (mA/cm^2), 48/59 (%), 3.1/5.2 (%), respectively. (B) External quantum efficiency (EQE) measurements of CIGS TF and CIGS NTRs solar cells, respectively.

4. Conclusions

In this study, the sequential experiments regarding how the ion sputtering duration effects on CIGS NTRs length to the effects of KCN treatment duration and buffer layer thickness were demonstrated. It was found out that the longest length could be obtained at the ion milling time of 30 min. According to GIXRD, EDS and AES analysis, the formation mechanism of CIGS NTRs was proposed to be self-masking effect by Cu-rich phase formed at an early stage of ion milling process. Note that GIXRD shows CIGS NTRs sample remains in chalcopyrite phase throughout the whole process. The best device efficiency could be obtained with the open circuit voltage and short circuit current were ~390 mV and ~22.56 mA/cm^2, yielding the FF and the efficiency of 59% and 5.2%, respectively. In contrast to CIGS TF solar cell with efficiency of 3.2%, the nanostructured CIGS NTRs can have efficiency enhancement of 60% due to the higher light absorption ability because of the nanostructure.

Acknowledgment

The authors gratefully thanks the National Science Council, Taiwan under the Grant of NSC 101-2218-E-007-009-MY3, 101-2622-E-007-011-CC2, and 101-2622-E-492-001-CC2, and the National Tsing Hua University under Grant No. 102N2022E1 for their financial support. Y. L. Chueh greatly appreciates the use of facility at CNMM at the National Tsing Hua University through Grant No. 101N2744E1.

References

[1] M.A. Green, K. Emery, Y. Hishikawa, W. Warta, E.D. Dunlop, Prog. Photovoltaics 20 (2012) 12.
[2] T. Dullweber, G.H. anna, U. Rau, H.W. Schock, Sol. Energy Mater. Sol. Cells, 67, 2001. 145.
[3] M. Topic, F. Smole, J. Furlan, J. Appl. Phys. 79 (1996) 8537.
[4] Z. Jehl, F. Erfurth, N. Naghavi, L. Lombez, I. Gerard, M. Bouttemy, P. Tran-Van, A. Etcheberry, G. Voorwinden, B. Dimmler, W. Wischmann, M. Powalla, J.F. Guillemoles, D. Lincot, Thin Solid Films 519 (2011) 7212.
[5] J.H. Zhao, A.H. Wang, M.A. Green, F. Ferrazza, J. Appl. Phys. 73 (1998) 1991.
[6] J. Zhu, C.-M. Hsu, Z. Yu, S. Fan, Y. Cui, Nano Lett. 10 (2009) 1979.
[7] Y. Ogawa, A. Jäger-Waldau, T.H. Hua, Y. Hashimoto, K. Ito, Appl. Surf. Sci. 92 (1996) 232.
[8] R. Klenk, R. Menner, D. Cahen, H.W. Schock, 1, 1990, p. 481.
[9] T. Negami, Y. Hashimoto, S. Nishiwaki, Sol. Energy Mater. Sol. Cells 67 (2001) 331.
[10] K. Orgassa, U. Rau, Q. Nguyen, H. Werner Schock, J.H. Werner, Prog. Photovoltaics 10 (2002) 457.
[11] R.M. Bradley, J.M.E. Harper, J. Vac. Sci. Technol. A 6 (1988) 2390.
[12] P. Sigmund, Phys. Rev. 184 (1969) 383.
[13] X.X. Liu, J.R. Sites, J. Appl. Phys. 75 (1994) 577.